Draft version March 16, 2023
Typeset using LaTeX twocolumn style in AASTeX61

FREE-FLOATING PLANET MASS FUNCTION FROM MOA-II 9-YEAR SURVEY TOWARDS THE GALACTIC BULGE

Takahiro Sumi,[1] Naoki koshimoto,[2,3] David P. Bennett,[2,3] Nicholas J. Rattenbury,[4] Fumio Abe,[5] Richard Barry,[2] Aparna Bhattacharya,[2,3] Ian A. Bond,[6] Hirosane Fujii,[5] Akihiko Fukui,[7,8] Ryusei Hamada,[9] Yuki Hirao,[9] Stela Ishitani Silva,[10,2] Yoshitaka Itow,[5] Rintaro Kirikawa,[9] Iona Kondo,[9] Yutaka Matsubara,[5] Shota Miyazaki,[9] Yasushi Muraki,[5] Greg Olmschenk,[2] Clément Ranc,[11] Yuki Satoh,[9] Daisuke Suzuki,[9] Mio Tomoyoshi,[9] Paul . J. Tristram,[12] Aikaterini Vandorou,[2,3] Hibiki Yama,[9] and Kansuke Yamashita[9]
(MOA collaboration)

[1] *Department of Earth and Space Science, Graduate School of Science, Osaka University, Toyonaka, Osaka 560-0043, Japan. e-mail:* sumi@ess.sci.osaka-u.ac.jp
[2] *Code 667, NASA Goddard Space Flight Center, Greenbelt, MD 20771, USA*
[3] *Department of Astronomy, University of Maryland, College Park, MD 20742, USA*
[4] *Department of Physics, University of Auckland, Private Bag 92019, Auckland, New Zealand*
[5] *Institute for Space-Earth Environmental Research, Nagoya University, Nagoya 464-8601, Japan*
[6] *Institute of Natural and Mathematical Sciences, Massey University, Auckland 0745, New Zealand*
[7] *Department of Earth and Planetary Science, Graduate School of Science, The University of Tokyo, 7-3-1 Hongo, Bunkyo-ku, Tokyo 113-0033, Japan*
[8] *Instituto de Astrofísica de Canarias, Vía Láctea s/n, E-38205 La Laguna, Tenerife, Spain*
[9] *Department of Earth and Space Science, Graduate School of Science, Osaka University, Toyonaka, Osaka 560-0043, Japan*
[10] *Department of Physics, The Catholic University of America, Washington, DC 20064, USA*
[11] *Sorbonne Université, CNRS, UMR 7095, Institut d'Astrophysique de Paris, 98 bis bd Arago, 75014 Paris, France*
[12] *University of Canterbury Mt. John Observatory, P.O. Box 56, Lake Tekapo 8770, New Zealand*

ABSTRACT

We present the first measurement of the mass function of free-floating planets (FFP) or very wide orbit planets down to an Earth mass, based on microlensing data from the MOA-II survey in 2006-2014. The shortest duration event has an Einstein radius crossing time of $t_{\rm E} = 0.057 \pm 0.016$ days and an angular Einstein radius of $\theta_{\rm E} = 0.90 \pm 0.14\,\mu$as. There are seven short events with $t_{\rm E} < 0.5$ day, which are likely to be due to planets. The detection efficiency for short events depends on both $t_{\rm E}$ and $\theta_{\rm E}$, and we measure this with image-level simulations for the first time. These short events can be well modeled by a power-law mass function, $dN_4/d\log M = (2.18^{+0.52}_{-1.40}) \times (M/8\,M_\oplus)^{-\alpha_4}$ dex^{-1}star^{-1} with $\alpha_4 = 0.96^{+0.47}_{-0.27}$ for $M/M_\odot < 0.02$. This implies a total of $f = 21^{+23}_{-13}$ FFP or wide orbit planets in the mass range $0.33 < M/M_\oplus < 6660$ per star, with a total FFP mass of $m = 80^{+73}_{-47} M_\oplus$ per star. The number of FFP is 19^{+23}_{-13} times the number of planets in wide orbits (beyond the snow line), while the total masses are of the same order. This suggests that the FFPs have been ejected from bound planetary systems that may have had an initial mass function with a power-law index of $\alpha \sim 0.9$, which would imply a total number of 22^{+23}_{-13} planets star^{-1} and a total mass of $171^{+80}_{-52} M_\oplus$ star^{-1}.

Keywords: gravitational microlensing; exoplanet; Free floating planets

1. INTRODUCTION

Gravitational microlensing observations toward the Galactic bulge (Galactic Bulge) enable exoplanet searches (Mao & Paczyński 1991; Gaudi et al. 2008; Bennett et al. 2010; Suzuki et al. 2016; Koshimoto et al. 2021b), and the measurement of the stellar and substellar mass functions (MFs) (Paczyński 1991; Sumi et al. 2011; Mróz et al. 2017, 2019, 2020a).

Sumi et al. (2011) first interpreted the detection of short timescale ($0.5 < t_{\rm E}/{\rm day} < 2$) microlensing events as evidence for the existence of a population of free-floating planets (FFP) and/or wide orbit planets. While that analysis was limited by the small number of events found in a 2 year subset of the survey by the Microlensing Observation in Astrophysics (MOA) group (Sumi et al. 2003) in collaboration with Optical Gravitational Lensing Experiment (OGLE) (Udalski et al. 1994), it opened up the field of FFP studies using microlensing.

Mróz et al. (2017) extended the work by using a larger sample from 5 years of the OGLE survey. They discovered 6 events with timescales shorter ($t_{\rm E} \sim 0.2$ day) than those in the previous work. These events are separated from the longer events by a gap around $t_{\rm E} \sim 0.5$ day which implying the possibility of a several Earth-mass FFP population.

These studies are based on distribution of $t_{\rm E}$, in which $t_{\rm E}$ is proportional to the square root of the lens mass M as follows,

$$\begin{aligned} t_{\rm E} &= \frac{\sqrt{\kappa M \pi_{\rm rel}}}{\mu_{\rm rel}} \\ &= 0.1\,{\rm day} \left(\frac{M}{5M_\oplus}\right)^{1/2} \left(\frac{\pi_{\rm rel}}{18\mu{\rm as}}\right)^{1/2} \left(\frac{\mu_{\rm rel}}{5{\rm mas\,yr^{-1}}}\right)^{-1}. \end{aligned} \tag{1}$$

Here, $\kappa = 4G/(c^2{\rm au}) = 8.144{\rm mas}/M_\odot$ and we expect $t_{\rm E} \sim 0.1$ day assuming typical value of the lens-source relative parallax: $\pi_{\rm rel} = \pi_{\rm l}^{-1} - \pi_{\rm s}^{-1} = 1\,{\rm au}(D_{\rm l}^{-1} - D_{\rm s}^{-1}) = 18\mu{\rm as}$ for the bulge lens and a typical value of the lens-source proper motion in the direction of the Galactic center of $\mu_{\rm rel} = 5\ {\rm mas\,yr^{-1}}$. The lens mass M, the distance $D_{\rm l}$ to the lens and the relative proper motion $\mu_{\rm rel}$ are degenerate in the observable $t_{\rm E}$. This means that the mass function of the lens population has to be determined statistically, assuming a model of the star population density and velocities in the Galaxy.

Mróz et al. (2018) found the first short ($t_{\rm E} = 0.32$ day) event showing the Finite Source (FS) effect, i.e., a finite source and a single point lens (FSPL), in which one can measure a FS parameter $\rho = \theta_*/\theta_{\rm E}$. Here θ_* is the angler source radius which can be estimated from an empirical relation with the source magnitude and color. The $\theta_{\rm E}$ is an angular Einstein radius given by

$$\theta_{\rm E} = \frac{\mu_{\rm rel}}{t_{\rm E}} = \sqrt{\kappa M \pi_{\rm rel}}. \tag{2}$$

This value of $\theta_{\rm E}$ can give us an inferred mass of the lens with better accuracy as we can eliminate one of the three-fold degenerate terms which affecte $t_{\rm E}$, namely, $\mu_{\rm rel}$:

$$M = \frac{\theta_{\rm E}^2}{\kappa \pi_{\rm rel}} = 5M_\oplus \left(\frac{\theta_{\rm E}}{1.5\mu{\rm as}}\right)^2 \left(\frac{\pi_{\rm rel}}{18\mu{\rm as}}\right)^{-1}. \tag{3}$$

So far, seven short FSPL events have been discovered (Mróz et al. 2018, 2019b, 2020b,c; Kim et al. 2021; Ryu et al. 2021). All of these have $\theta_{\rm E} < 10\,\mu$as, implying that their lenses are most likely of planetary mass. All of these sources are red giants because their angular radii, i.e., cross-section, are significantly larger than main sequence stars.

Mróz et al. (2020b) found the short FSPL event, OGLE-2016-BLG-1928, with the smallest value of $\theta_{\rm E} = 0.842 \pm 0.064\mu$as to date. Its lens is the first terrestrial mass FFP candidate and the first evidence of such population.

Kim et al. (2021) began a new approach to probing the FFP population by focusing on analyzing the $\theta_{\rm E}$ distribution in events with giant sources. Ryu et al. (2021) found a gap at $10 < \theta_{\rm E}/\mu{\rm as} < 30$ in the cumulative $\theta_{\rm E}$ distribution, which suggests a separation between the planetary mass population and other known populations, like brown dwarfs.

Gould et al. (2022) completed the analysis of 29 FSPL giant-source events found in the 2016-2019 KMTNet survey. They presented the $\theta_{\rm E}$ distributions down to $\theta_{\rm E} = 4.35\,\mu$as and confirmed that there is a clear gap in the distribution of $\theta_{\rm E}$ at $9 < \theta_{\rm E}/\mu{\rm as} < 26$. They note that it is consistent with the gap in the $t_{\rm E}$ distribution shown by Mróz et al. (2017), indicating the existence of the low mass FFP population. They modeled the $\theta_{\rm E}$ distribution with a power law MF for the FFP and found $dN_{\rm FFP}/d\log M = (0.4 \pm 0.2)(M/38M_\oplus)^{-p}$ ${\rm dex^{-1}\,star^{-1}}$, with $0.9 < p < 1.2$. This implies that the number of FFPs is at least an order of magnitude larger than that for known bound planets.

In this paper, we present the distributions $\theta_{\rm E}$ and $t_{\rm E}$ values for the microlensing events toward the Galactic Bulge from 9 years of the MOA-II survey. We also present the MF of the planetary mass objects using the $t_{\rm E}$ distribution. We describe the data in section § 2. We show the $\theta_{\rm E}$ distribution in section § 3. We present the $t_{\rm E}$ distribution and the best-fit MF in § 4. The discussion and conclusions are given in section § 5.

2. DATA

We use the microlensing sample selected from the MOA-II high cadence photometric survey toward the Galactic Bulge in the 2006-2014 seasons (Koshimoto et al. 2023, hereafter K23). MOA-II uses the 1.8-m MOA-II telescope which has a 2.18 deg^2 field of view (FOV) and which is located at the Mt. John University Observatory, New Zealand[1].

K23 used an analysis method similar to what was used by Sumi et al. (2011, 2013), but includes a correction of systematic errors and takes into account the finite source effect. They applied a de-trending code to all light curves to remove the systematic errors that correlate with seeing and airmass due to differential refraction, differential extinction and relative proper motion of stars in the same way as in Bennett et al. (2012) and Sumi et al. (2016a). These corrections are important as they result in higher confidence in the light curve fitting parameters.

K23 selected light curves with a single instantaneous brightening episode and a flat constant baseline, which can be well fit with a point-source point-lens (PSPL) microlensing model (Paczyński 1986). In addition to PSPL, they modeled the events with a FSPL model (Bozza et al. 2018), which is especially important for short events. These are the major improvements compared to the previous analysis in Sumi et al. (2011, 2013) in addition to the extension of the survey duration.

Although they identified 6,111 microlensing candidates, they selected only 3,554 and 3,535 objects as the statistical sample using the two relatively strict criteria CR1 and CR2, respectively. Here, CR2 was defined as the stricter criteria compared to their nominal criteria CR1 to check the effect of the choice of the criteria on a statistical study. These strict criteria ensure that $t_{\rm E}$ is well constrained for each event and reject any contamination.

Sumi et al. (2011) reported 10 short events with $t_{\rm E} < 2$ days in the 2006-2007 dataset. Only 5 and 4 events survived following the application of CR1 and CR2, respectively. This is because the fitting results changed due to the re-reduction of the dataset. On the other hand, two events are newly found resulting 7 and 6 events following the application of CR1 and CR2, respectively. As a result, the excess at $t_{\rm E} = 0.5 - 2$ day in the $t_{\rm E}$ distribution is not significant anymore, however, an even shorter event MOA-9y-6057 ($t_{\rm E} = 0.22 \pm 0.06$ day) is added.

3. ANGULAR EINSTEIN RADIUS DISTRIBUTION

[1] https://www.massey.ac.nz/~iabond/moa/alerts/

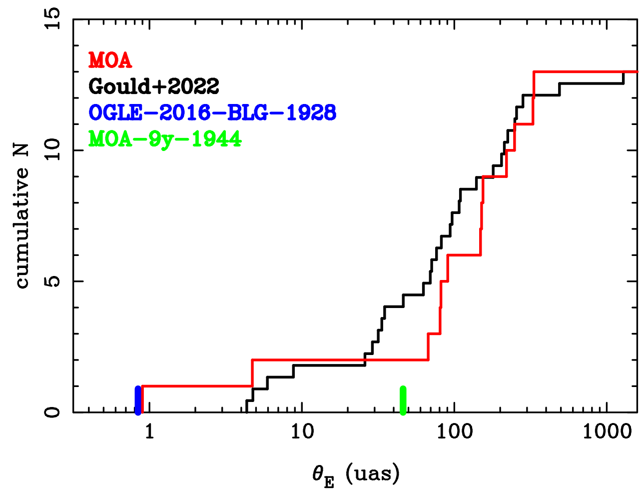

Figure 1. Observed cumulative distribution of $\theta_{\rm E}$ for 13 FSPL events from MOA (red line) and 29 FSPL events from KMTNet (black line) (Gould et al. 2022). The blue line indicates $\theta_{\rm E} = 0.842 \pm 0.064$ of terrestrial mass FFP candidate, OGLE-2016-BLG-1928 (Mróz et al. 2020b).

There are 13 FSPL events with $\theta_{\rm E}$ measurements in the sample, including two FFP candidates, MOA-9y-5919 and MOA-9y-770, that have terrestrial and Neptune masses, respectively. See K23 for the light curves and detailed parameters of the 13 events.

The red line in Figure 1 indicates the cumulative distribution of $\theta_{\rm E}$ from Table 7 of K23. The black line indicates the distribution of 29 FFPs by Gould et al. (2022) normalized to 13 events as a comparison. Although these can not be directly compared because these are not corrected for detection efficiencies, the general trends seen Figure 1 may give us some insights.

The distributions are consistent for $\theta_{\rm E} > 30\,\mu$as, where the effect of the detection efficiencies are likely small. There is a gap around $5 < \theta_{\rm E}/\mu{\rm as} < 70$ which is roughly consistent with the gap at $10 < \theta_{\rm E}/\mu{\rm as} < 30$ found by Ryu et al. (2021) and Gould et al. (2022). This gap confirmed the existence of the planetary mass population as distinct and separated from the stellar/brown dwarf population as indicated by Gould et al. (2022).

The MOA cumulative distribution shows fewer events over $30 < \theta_{\rm E}/\mu{\rm as} < 70$ compared to Gould et al. (2022). This may be just due to the small number of statistics. But note that K23 found a brown dwarf candidate MOA-9y-1944 with $\theta_{\rm E} = 46.1 \pm 10.5\,\mu$as although this is not in the final sample for statistical analysis because the source magnitude of $I_{\rm s} = 21.91$ mag is fainter than the threshold of $I_{\rm s} < 21.4$ mag.

In our sample, there is one event with a very small value of $\theta_{\rm E}$ of $0.90 \pm 0.14\,\mu$as. This confirms the existence

Table 1. Comparison of parameters of short FS events with known FFP candidates.

field-chip-sub-ID	t_E (day)	ρ	$I_{s,0}$ (mag)	θ_* (μas)	θ_E (μas)	reference
MOA-9y-5919	0.057 ± 0.016	1.40 ± 0.46	17.23	1.26 ± 0.48	0.90 ± 0.14	K23
MOA-9y-770	0.315 ± 0.017	1.08 ± 0.07	14.71	5.13 ± 0.86	4.73 ± 0.75	K23
OGLE-2016-BLG-1928	$0.0288^{+0.0024}_{-0.0016}$	$3.39^{+0.10}_{-0.11}$	15.78	2.85 ± 0.20	0.842 ± 0.064	Mróz et al. (2020b)
KMT-2019-BLG-2073	0.272 ± 0.007	1.138 ± 0.012	14.45	5.43 ± 0.17	4.77 ± 0.19	Kim et al. (2021)
KMT-2017-BLG-2820	0.288 ± 0.015	1.096 ± 0.079	14.31	7.05 ± 0.44	5.94 ± 0.37	Ryu et al. (2021)
OGLE-2012-BLG-1323	0.155 ± 0.005	5.03 ± 0.07	14.09	11.9 ± 0.5	2.37 ± 0.10	Mróz et al. (2019b)
OGLE-2016-BLG-1540	0.320 ± 0.003	1.65 ± 0.01	13.51	15.1 ± 0.8	9.2 ± 0.5	Mróz et al. (2018)
OGLE-2019-BLG-0551	0.381 ± 0.017	4.49 ± 0.15	12.61	19.5 ± 1.6	4.35 ± 0.34	Mróz et al. (2020c)
MOA-9y-1944[a]	1.594 ± 0.136	0.00928 ± 0.00032	20.14	0.43 ± 0.10	46.1 ± 10.5	K23
OGLE-2017-BLG-0560[a]	0.905 ± 0.005	0.901 ± 0.005	12.47	34.9 ± 1.5	38.7 ± 1.6	Mróz et al. (2019b)

[a] Likely Brown dwarf lens.

of the terrestrial mass population which gives rise to events such as OGLE-2016-BLG-1928 which has $\theta_E = 0.842 \pm 0.064$ (Mróz et al. 2020b). These values are significantly smaller than the lower edge of $\theta_E \sim 4.35\,\mu$as as reported in Gould et al. (2022). This is likely a result of selection bias given that Gould et al. (2022) focused on the sample with super-giant sources, see Figure 2.

We compare the parameters of these events to seven known FFP candidates with θ_E measurements in Table 1. The sources of all known FFP candidates except OGLE-2016-BLG-1928 are red clump giants (RCGs) or red super-giants which have large $\theta_* = 5.4, 7.1, 11.9, 15.1, 19.5$ and $34.9\,\mu$as. The magnification tend to be suppressed by large θ_* with small θ_E, i.e., large ρ as $A_{FS,max} = \sqrt{1 + 4/\rho^2}$ ($\rho > 1$) (Maeder 1973; Agol 2003; Riffeser et al. 2006). For example, in case of the terrestrial mass lens with $\theta_E \sim 1\mu$as, the maximum magnification will be only $A_{FS,max} = 1.066, 1.039, 1.014, 1.009, 1.005$ and 1.002 for the above values of θ_*, respectively. Note that the source of the terrestrial FFP candidate event, OGLE-2016-BLG-1928S is a sub-giant with $\theta_* = 2.37\,\mu$as. It is important to search for short FSPL with sub-giants and dwarf sources to find low mass FFP. There is no FSPL event with a red super-giant source in our sample because these are saturated in MOA image data.

K23 provides the detection efficiency for our FSPL event sample to compare to those in Gould et al. (2022) who tried to constrain the FFP MF from only θ_E distribution for their FSPL event sample. However, we perform a likelihood analysis using not only θ_E of the FSPL events, but also include t_E of PSPL events which are more informative than θ_E distribution alone. See more details in Section 4.

4. LIKELIHOOD ANALYSIS OF MASS FUNCTION

In the final sample of K23, there are 10 (12) short timescale events with $t_E < 1$ day after applying CR2 (CR1). Figure 3 shows the t_E distribution of the CR2 sample. The distribution is roughly symmetric in $\log t_E$, with a tail at $t_E < 0.5$. This confirmed the existence of such short timescale events with $t_E < 0.5$ day as reported by Mróz et al. (2017). In this section, we perform a likelihood analysis on each of the 3554 (CR1) and 3535 (CR2) events using a Galaxy model to constrain the mass function of lens objects.

We define the likelihood, $\mathcal{L}$, in Section 4.1. In Sections 4.2 and 4.3, we determine the mass function without and with a planetary mass population, respectively, by minimizing $\chi^2 \equiv -2\ln\mathcal{L}$. Although the absolute value of χ^2 is not meaningful due to its dependence on an arbitrary normalization associated with our likelihood calculation, the fitting procedure is still statistically valid as the relative likelihood between two models, represented by $\Delta\chi^2$, is independent of the normalization.

Note that results of the likelihood analysis for sample CR1 and CR2 are very similar. In the following sections, we show only the results for CR2 as our final results except in the tables.

4.1. *Likelihood*

Although our sample contains more than 3500 events, the mass function of planetary-mass objects is largely determined by the events with $t_E < 1$ day, which account for about 0.3% of them. We separately define two likelihoods; $\mathcal{L}_{short}$ for short timescale events with the best-fit $t_E < 1$ day, and $\mathcal{L}_{long}$ for events with the best-fit $t_E \geq 1$ day. In our likelihood analysis, we use the combined likelihood of $\mathcal{L} = \mathcal{L}_{short}\mathcal{L}_{long}$.

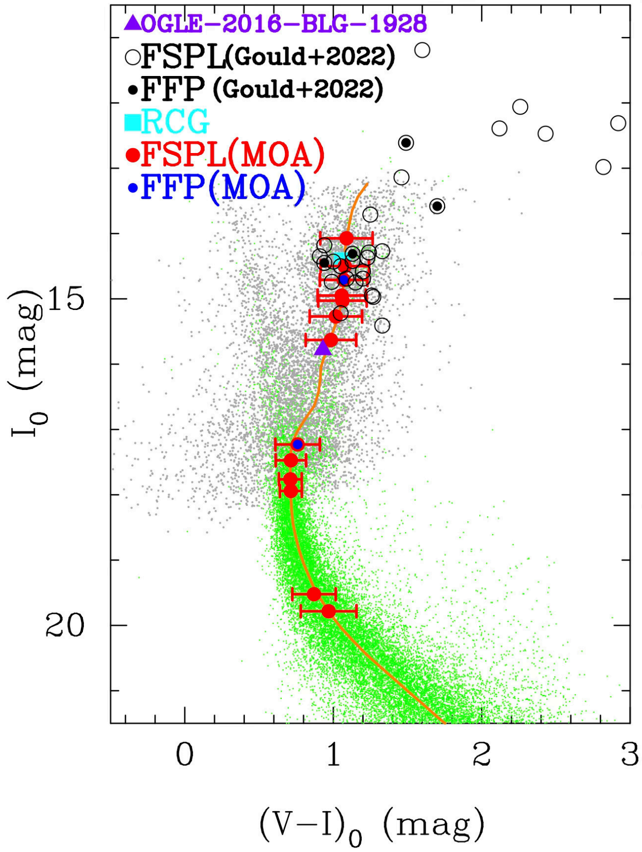

Figure 2. Extinction free CMD of gb3-7-6. The orange curve is the isochrone matched to this subfield. The cyan square is the RCG centroid. The red circles with error bars are sources of the 13 FSPL events in this work. The blue filled circles indicates the 2 FFP candidates in this work. The black open and filled circles are FSPL events and FFP events from Gould et al. (2022), respectively. The purple triangle indicates the source of terrestrial FFP, OGLE-2016-BLG-1928S (Mróz et al. 2020b).

For $\mathcal{L}_{\rm long}$, we simply use the best-fit $t_{\rm E}$ values provided by K23, which is similar to the approach by previous studies (Sumi et al. 2011; Mróz et al. 2017). This is because (i) the relatively smaller errors of $t_{\rm E}$, (ii) the effect of individual $t_{\rm E}$ error is statistically marginalized by the large number of events, (iii) the limited sensitivity to $\theta_{\rm E}$, and (iv) the minimal impact on our primary goal of measuring the mass function of planetary mass objects.

On the other hand, the situation is the opposite for the short events, $\mathcal{L}_{\rm short}$, i.e., (i) the $t_{\rm E}$ errors are relatively large due to their shorter magnification period, although smaller than the event selection threshold (see Table 2 of K23), (ii) the number of events is very limited (12 for CR1 and 10 for CR2), and $t_{\rm E} < 1$ day is only sparsely covered in Figure 3. Thus, these may not be sufficient

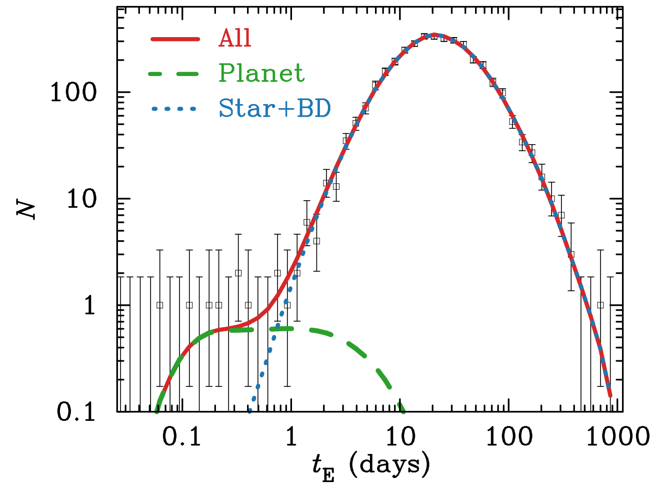

Figure 3. The observed timescale $t_{\rm E}$ distribution passing criteria CR2 from the 9 year MOA-II survey.. The red line indicates the best fit single lens model for all population. The blue dotted line represents the known populations of stars, brown dwarfs, and stellar remnants, and the green dashed line represents the planetary mass population.

to statistically marginalize the effect of $t_{\rm E}$ errors of individual events in the likelihood analysis, (iii) because $\rho = \theta_*/\theta_{\rm E}$ are expected to be larger than those of longer timescale events, one may get beneficial constraints on $\theta_{\rm E}$ even if $\theta_{\rm E}$ are not well determined, and (iv) they play a crucial role in determining the mass function of planetary mass objects. Therefore, we use the joint posterior probability distribution of $(t_{\rm E}, \theta_{\rm E})$ for each event derived by K23 using the Markov Chain Monte Carlo (MCMC) method for $\mathcal{L}_{\rm short}$, to take into account both $t_{\rm E}$ and $\theta_{\rm E}$ information and their uncertainties.

We first describe the simpler one, $\mathcal{L}_{\rm long}$, in Section 4.1.1, then describe $\mathcal{L}_{\rm short}$ in Section 4.1.2.

4.1.1. *Likelihood for events with $t_{\rm E} \geq 1$ day*

We define the likelihood for events with $t_{\rm E} \geq 1$ day by

$$\mathcal{L}_{\rm long} \propto \prod_{i=1}^{N_{\rm long}} \mathcal{G}(t_{{\rm E},i}; \Gamma), \tag{4}$$

where i runs over all the $N_{\rm long}$ events that have the best-fit $t_{\rm E} \geq 1$ day in our sample ($N_{\rm long} = 3542$ for CR1 and $N_{\rm long} = 3525$ for CR2), and $t_{{\rm E},i}$ is the best-fit $t_{\rm E}$ value for ith event given by K23.

The function $\mathcal{G}(t_{\rm E}; \Gamma)$ is the model's detectable event rate as a function of $t_{\rm E}$ with given model event rate Γ, combined for the 20 survey fields, given by

$$\mathcal{G}(t_{\rm E}; \Gamma) = \sum_j w_j \, g_j(t_{\rm E}; \Gamma_j). \tag{5}$$

Here, j takes field index values gb1 to gb21, except for gb6. See Table 1 of K23 for the location and properties of each field. The weight w_j for the jth field is given by

$$w_j = \sum_{k\in j} n^2_{\mathrm{RC},k} f_{\mathrm{LF},k}, \tag{6}$$

where k indicates a 1024 pixel × 1024 pixel subframe in the jth field ($k = 1, 2, ..., 80$), $n_{\mathrm{RC},k}$ is the number density of RCGs in the kth subfield, $f_{\mathrm{LF},k}$ is the fraction of stars with magnitude $I < 21.4$ mag in the kth subfield, and w_j is thus proportional to the expected event rate in the jth field. To calculate $f_{\mathrm{LF},k}$, we used a combined luminosity function that uses the OGLE-III photometry map (Szymański 2011) for bright stars and the *Hubble Space Telescope* data by (Holtzman et al. 1998) for faint stars.

The function g_j is the model's detectable event rate as a function of t_{E} for field j as given by

$$g_j(t_{\mathrm{E}};\Gamma_j) = \tilde{\epsilon}_j(t_{\mathrm{E}};\Gamma_j)\,\Gamma_j(t_{\mathrm{E}}), \tag{7}$$

where $\tilde{\epsilon}(t_{\mathrm{E}};\Gamma)$ is the integrated detection efficiency of the survey as a function of t_{E}. K23 demonstrated that when finite source effects are important, the detection efficiency, $\epsilon(t_{\mathrm{E}}, \theta_{\mathrm{E}})$ is a function of two variables, t_{E} and θ_{E}. Therefore, we must integrate over θ_{E} to obtain the integrated detection efficiency, $\tilde{\epsilon}(t_{\mathrm{E}};\Gamma)$, which now depends upon the event rate and the mass function of the lens objects. This gives

$$\tilde{\epsilon}_j(t_{\mathrm{E}};\Gamma) = \int_{\theta_{\mathrm{E}}} \epsilon_j(t_{\mathrm{E}}, \theta_{\mathrm{E}})\,\Gamma_j(\theta_{\mathrm{E}}|t_{\mathrm{E}})d\theta_{\mathrm{E}}, \tag{8}$$

where $\epsilon_j(t_{\mathrm{E}}, \theta_{\mathrm{E}})$ is the detection efficiency for events with t_{E} and θ_{E} for ith field. We use the detection efficiency $\epsilon_j(t_{\mathrm{E}}, \theta_{\mathrm{E}})$ estimated by the image level simulations in K23 for the 20 fields of the MOA-II 9-yr survey.

We consider the model event rate as a function of t_{E} and $(t_{\mathrm{E}}, \theta_{\mathrm{E}})$, $\Gamma(t_{\mathrm{E}})$ and $\Gamma(t_{\mathrm{E}}, \theta_{\mathrm{E}})$, respectively, as a normalized function so that its integration gives one, i.e., these are probability density functions of t_{E} and $(t_{\mathrm{E}}, \theta_{\mathrm{E}})$, respectively. $\Gamma(\theta_{\mathrm{E}}|t_{\mathrm{E}}) = \Gamma(t_{\mathrm{E}}, \theta_{\mathrm{E}})/\Gamma(t_{\mathrm{E}})$ is the probability density of events with θ_{E} given t_{E}. Thus, the calculation of $\tilde{\epsilon}(t_{\mathrm{E}};\Gamma)$ in Eq. (8) has to be done for every proposed MF during the fitting procedure because $\Gamma(\theta_{\mathrm{E}}|t_{\mathrm{E}})$ depends on the MF.

The function $\Gamma_j(t_{\mathrm{E}}, \theta_{\mathrm{E}})$ for jth field can be separated from the MF (Han & Gould 1996),

$$\Gamma_j(t_{\mathrm{E}}, \theta_{\mathrm{E}}) = \int \gamma_j(t_{\mathrm{E}}M^{-1/2}, \theta_{\mathrm{E}}M^{-1/2})\Phi(M)\sqrt{M}dM, \tag{9}$$

where $\gamma_j(t_{\mathrm{E}}, \theta_{\mathrm{E}})$ is the event rate for lenses with mass $1\,M_\odot$ and $\Phi(M)$ is the present-day MF (expressed as dN/dM). Although substituting Eqs. (8) and (9) makes the calculation of $g_j(t_{\mathrm{E}};\Gamma_j)$ in Eq. (7) a double integral over M and θ_{E}, K23 showed that the integration over θ_{E} is largely avoidable during a fitting procedure by switching the order of the integrals and calculating the integral over θ_{E} before the fitting.

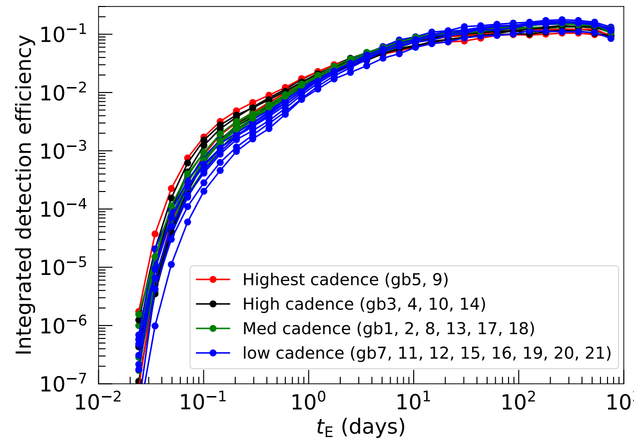

Figure 4. Integrated detection efficiencies, $\tilde{\epsilon}(t_{\mathrm{E}};\Gamma)$, as a function of the timescale t_{E} down to the source magnitude of $I_{\mathrm{s}} < 21.4$ mag for the criteria CR2. Red, black, green and blue lines indicate the efficiencies of fields with the highest, high, medium and low cadence, respectively.

We calculate $\gamma_j(t_{\mathrm{E}}, \theta_{\mathrm{E}})$ for each field using the density and velocity distribution of stars from the latest parametric Galactic model toward the Galactic Bulge based on Gaia and microlensing data (Koshimoto et al. 2021a).

Figure 4 shows the integrated detection efficiencies $\tilde{\epsilon}(t_{\mathrm{E}};\Gamma)$ for the event rate calculated with the best fit MF model with the criteria CR2. The curve for CR1 is similar.

4.1.2. *Likelihood for short timescale ($t_{\mathrm{E}} < 1$ day) events*

We follow Hogg et al. (2010) to utilize the posterior probability distribution of each event from MCMC to calculate the likelihood for the short timescale events, $\mathcal{L}_{\mathrm{short}}$. Given the output MCMC samples of posterior distributions for individual events by K23, the likelihood is presented by

$$\mathcal{L}_{\mathrm{short}} \propto \prod_{i=1}^{N_{\mathrm{short}}} \sum_{k=1}^{K_i} \frac{\mathcal{G}(\log t_{\mathrm{E},ik}, \log\theta_{\mathrm{E},ik};\Gamma)}{p_0(\log t_{\mathrm{E},ik}, \log\theta_{\mathrm{E},ik})}, \tag{10}$$

where i runs over all the N_{short} events that have the best-fit $t_{\mathrm{E}} < 1$ day ($N_{\mathrm{short}} = 12$ for CR1 and $N_{\mathrm{short}} = 10$ for CR2), k runs over all the K_i samples in the MCMC sample of posterior distribution for ith event, and $p_0(\log t_{\mathrm{E}}, \log\theta_{\mathrm{E}})$ is the prior distribution multiplied

in the posterior. The model's detectable event rate as a function of $(\log t_{\rm E}, \log \theta_{\rm E})$ is given by

$$\mathcal{G}(\log t_{\rm E}, \log \theta_{\rm E}; \Gamma) = \sum_j w_j \, g_j(\log t_{\rm E}, \log \theta_{\rm E}; \Gamma_j) \quad (11)$$

with

$$g_j(\log t_{\rm E}, \log \theta_{\rm E}; \Gamma_j) = \epsilon_j(\log t_{\rm E}, \log \theta_{\rm E}) \, \Gamma_j(\log t_{\rm E}, \log \theta_{\rm E}), \quad (12)$$

where we represented it as a function of $(\log t_{\rm E}, \log \theta_{\rm E})$ rather than $(t_{\rm E}, \theta_{\rm E})$ because K23 provide the posterior distributions with the uniform prior in $(\log t_{\rm E}, \log \theta_{\rm E})$, i.e., $p_0(\log t_{\rm E}, \log \theta_{\rm E}) = {\rm const.}$.

Eq. (10) calculates the likelihood by summing the ratio of $\mathcal{G}(\log t_{\rm E}, \log \theta_{\rm E}; \Gamma)$ to $p_0(\log t_{\rm E}, \log \theta_{\rm E})$ to replace the used prior (i.e., p_0) with the new prior (i.e., $\mathcal{G}$) over the MCMC samples. This method, which uses all the MCMC samples, allows $\mathcal{L}_{\rm short}$ to account for the uncertainty of the parameters, unlike $\mathcal{L}_{\rm long}$ given in Eq. (4).

Despite the significant computational cost of Eq. (10) associated with performing a summation over K_i (typically $\sim 5 \times 10^5$) samples for each proposed mass function during the fitting process, we addressed this by implementing a binning strategy for the MCMC sample using grids of $(\log t_{\rm E}, \log \theta_{\rm E})$ with a size of (0.05 dex $\times$ 0.05 dex), which significantly increased the computational efficiency.

4.2. *Mass function of known population*

Firstly, we perform the likelihood analysis without the short events with $t_{\rm E} < 1$ day using the Galactic model with the MF of known population, i.e., stellar remnants (black holes (BH), neutron stars (NS) and white dwarfs(WD)), main sequence stars (MS) and brown dwarfs (BD). We use a broken power-law MF given by

$$\frac{dN}{d\log M} \propto \begin{cases} M^{-\alpha_1} & (M_1 < M/M_\odot < 120) \\ M^{-\alpha_2} & (0.08 < M/M_\odot < M_1) \\ M^{-\alpha_3} & (3 \times 10^{-4} < M/M_\odot < 0.08). \end{cases} \quad (13)$$

We adopt the values of parameters $\alpha_1 = 1.32$ and $\alpha_2 = 0.13$, $\alpha_3 = -0.82$ and $M_1 = 0.86$ from the E+E$_{\rm X}$ model of Koshimoto et al. (2021a) by default unless specified as fitting parameters in the following three models. The minimum mass $3 \times 10^{-4}\, M_\odot$ is taken to be smaller than the theoretical minimum mass of the gas cloud, $\sim$Jupiter-mass, that collapses to form a brown dwarf (Boss et al. 2003). During our fitting procedure, a proposed initial mass function (IMF) is converted into a present-day mass function following the procedure used by Koshimoto et al. (2021a) that combines their stellar age distribution and the initial-final mass relation by Lam et al. (2020) to evolve stars into stellar remnants.

We consider three models here: BD1, BD2, and BD3. In BD1, we fit only α_3 as a fitting parameter, while fixing α_1, α_2, and M_1. Similarly, in BD2, we fit α_3 and α_2, and in BD3, we fit α_1, α_2, α_3, and M_1. To perform the fitting, we use the Markov Chain Monte Carlo (MCMC) method (Metropolis et al. 1953), and assign uniform distributions as priors for all the parameters.

The best fit models BD1, BD2 and BD3 are almost indistinguishable from the blue dotted line in Figure 3. One can see that the models fit the data with $t_{\rm E} > 1$ day very well. The best fit parameters and χ^2 values are listed in Table 2. There is no significant difference in the resultant parameters between different selection criteria or among the BD1, BD2, and BD3 models.

All of the parameters are consistent with those of Koshimoto et al. (2021a) within 1σ. This indicates that our dataset confirmed the Galactic model and MF of known objects by Koshimoto et al. (2021a). This also indicates that our dataset is consistent with the OGLE-IV $t_{\rm E}$ distribution for $t_{\rm E} > 1$ day (Mróz et al. 2017, 2019) that is fitted by Koshimoto et al. (2021a).

In the following analysis, we fit only α_3 and fix all other parameters for the known populations. Note, in Koshimoto et al. (2021a), the Galactic model and MF are constrained to satisfy the microlensing $t_{\rm E}$ distribution, stellar number counts and the Galactic Bulge mass from other observations, simultaneously. In principle, the MF should not be changed alone because it is related to other parameters of the Galactic model. However, the contribution of objects with $M/M_\odot < 0.08$ are negligible in stellar number counts and as a fraction of the Galactic Bulge mass. Thus, we assume that a model with a different slope at lower masses with $M/M_\odot < 0.08$ is still valid.

4.3. *Mass function of planetary mass population*

If the candidates with $t_{\rm E} < 0.5$ day are really due to microlensing, they can not be explained by known populations, i.e., stellar remnants, MS or BD. To explain the tail for short values of $t_{\rm E}$, we defined a new model "PL" which introduces a planetary mass population by the following power law in addition to known populations (Eq. 13),

$$\frac{dN_4}{d\log M} = Z \left(\frac{M}{M_{\rm norm}} \right)^{-\alpha_4}, (M_{\rm min} < M/M_\odot < 0.02). \quad (14)$$

Here Z is a normalization factor and $M_{\rm norm}$ is a reference mass whose inclusion allows Z to have a unit

Table 2. Best fit parameters of the mass function for known population.

model	BD1		BD2		BD3		Koshimoto+21a[a]
	CR1	CR2	CR1	CR2	CR1	CR2	
M_1	(0.86)	(0.86)	(0.86)	(0.86)	$0.97^{-0.04}_{-0.34}$	$0.99^{-0.06}_{-0.37}$	$0.86^{+0.09}_{-0.10}$
α_1	(1.32)	(1.32)	(1.32)	(1.32)	$1.33^{+0.21}_{-0.17}$	$1.34^{+0.18}_{-0.18}$	$1.32^{+0.14}_{-0.10}$
α_2	(0.13)	(0.13)	$0.20^{+0.07}_{-0.05}$	$0.20^{+0.07}_{-0.05}$	$0.23^{+0.04}_{-0.19}$	$0.24^{+0.04}_{-0.21}$	$0.13^{+0.11}_{-0.12}$
α_3	$-0.60^{+0.08}_{-0.13}$	$-0.62^{+0.09}_{-0.14}$	$-0.74^{+0.13}_{-0.30}$	$-0.76^{+0.14}_{-0.30}$	$-0.76^{+0.19}_{-0.26}$	$-0.79^{+0.22}_{-0.25}$	$-0.82^{+0.24}_{-0.51}$
χ^2	35919.4	35722.6	35918.2	35721.5	35918.0	35721.3	

[a] Results of fitting to various bulge data including the OGLE-IV t_E distribution of $t_E > 1$ day (Mróz et al. 2017, 2019). The representative values are shifted to the ones for the E+E$_X$ model from their original ones for the G+G$_X$ model.

NOTE—Some of the upper errors of M_1 is negative because the best fit value is outside of the 68% range. This is because M_1 is restricted to be less than 1 $M_\odot$.

of $(\text{dex})^{-1}$. Although $M_{\rm norm}$ can be an arbitrary zero point, we found that the uncertainty in Z is minimized when we adopt $M_{\rm norm} = 8\,M_\oplus$ which is recognized as a pivot point.

In the model PL, we use α_3, α_4 and Z, as fitting parameters and fix parameters $\alpha_1 = 1.32$, $\alpha_2 = 0.13$ and $M_1 = 0.86$ (Koshimoto et al. 2021a). We assign uniform distributions as priors for α_3, α_4 and $\log Z$ in our MCMC run. We found that the fitting result does not depend on $M_{\rm min}$ at all when $M_{\rm min} < 3\times10^{-7}\,M_\odot$, which indicates our data sensitivity is down to $\sim 3\times10^{-7} M_\odot$. Thus, we decided to use $M_{\rm min} = 10^{-7}$.

The red solid line in Figure 3 represents the best fit model for all populations with the CR2 sample. This figure indicates that the model represents the observed t_E distribution well. Note that although the observed t_E distribution shown in black in Figure 3 does not include error bars along the t_E axis, the best-fit line is derived from our likelihood analysis that takes into account the t_E errors as well as the θ_E constraints for the short events with $t_E < 1$ day. Figure 5 shows the posterior distributions of the parameters of PL model. The best fit parameters and χ^2 are listed in Table 3.

The best fit power index for BD is $\alpha_3 = -0.58^{+0.12}_{-0.16}$ which is consistent with the model without the planetary mass population.

The best fit MF of the planetary mass populations with the normalization Z relative to stars (MS+BD+WD) (integrated IMF over $3\times10^{-4} < M/M_\odot < 8$) can be expressed as

$$\frac{dN_4}{d\log M} = \frac{2.18^{+0.52}_{-1.40}}{\text{dex}\times\text{star}}\left(\frac{M}{8\,M_\oplus}\right)^{-\alpha_4}, \qquad (15)$$

where $\alpha_4 = 0.96^{+0.47}_{-0.27}$. Figure 6 shows the IMF of the best fit PL model. This α_4 is consistent with the corresponding power law index of $0.9 \lesssim p \lesssim 1.2$ reported by Gould et al. (2022).

This can be translated to the normalization per stellar mass of stars, $Z^{M_\odot}$, as,

$$\frac{dN_4}{d\log M} = \frac{5.48^{+1.18}_{-3.50}}{\text{dex}\times M_\odot}\left(\frac{M}{8\,M_\oplus}\right)^{-\alpha_4}. \qquad (16)$$

This implies that the number of FFPs per stars is $f = 21^{+23}_{-13}\,\text{star}^{-1}$ over the mass range $10^{-6} < M/M_\odot < 0.02$. Note taht this value is vary depending on the minimum mass. The total mass of FFPs per star is $m = 80^{+73}_{-47}M_\oplus(0.25^{+0.23}_{-0.15}M_J)\,\text{star}^{-1}$. This is less dependent from the minimum mass. The total mass of FFPs per $M_\odot$ is $m^{M_\odot} = 202^{+166}_{-114}\,M_\oplus(0.64^{+0.19}_{-0.11}M_J)M_\odot^{-1}$. This is more robust values less dependent on uncertainty in the abundances of the low mass objects for both FFP and BD.

The normalization, number and total mass of FFP relative to MS+BD ($3\times10^{-4} < M/M_\odot < 1.1$) are also shown in Table 3. These normalizations can be translated to $Z_{\rm MS+BD} = 0.53^{+0.19}_{-0.40}\ \text{dex}^{-1}\text{star}^{-1}$ and $Z^{M_\odot}_{\rm MS+BD} = 2.44^{+0.71}_{-1.82}\ \text{dex}^{-1}M_\odot^{-1}$ with $M_{\rm norm} = 38M_\oplus$. These are almost same as $Z_{\rm MS+BD} = 0.39\pm0.18\ \text{dex}^{-1}\text{star}^{-1}$ and $Z_{\rm MS+BD} = 1.96\pm0.98\ \text{dex}^{-1}M_\odot^{-1}$ with $M_{\rm norm} = 38M_\oplus$ by Gould et al. (2022).

Note that the lenses for these short events could be either FFP or planets with very wide separations of more than about ten astronomical units (AU) from their host stars, for which we cannot detect the host star in the light curves.

5. DISCUSSION AND CONCLUSIONS

We derived the MF of lens objects from the 9-year MOA-II survey towards the Galactic Bulge. The 3,535 high quality single lens light curves used in our statistical analysis include 10 very short ($t_E < 1$ day) events, and

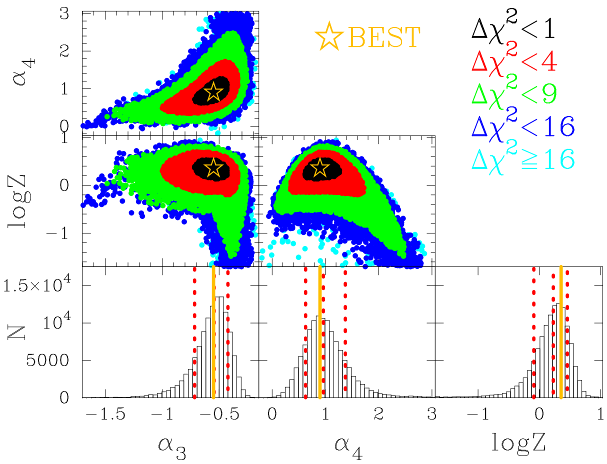

Figure 5. Posterior distributions of the parameters of the PL model for sample CR2. The vertical red dotted lines indicate the median and $\pm1\sigma$. The vertical orange line indicates the best fit.

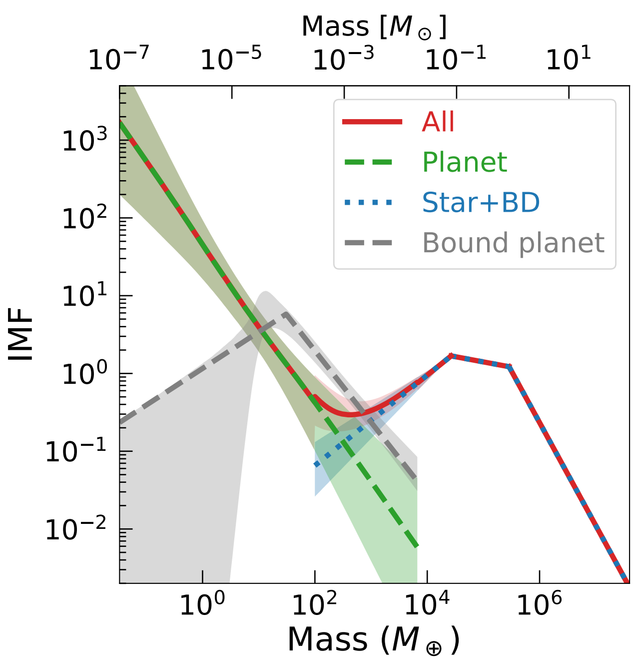

Figure 6. Initial mass function (IMF) of the best fit PL model for CR2. The red line indicates the best fit for all population. The blue dotted line and green dashed line show the IMFs for the stellar and brown dwarf population and for the planetary mass population, respectively. The shaded areas indicate 1σ error. The gray dashed-line and the shaded area indicate the best-fit and 1 σ range of the bound planet MF by Suzuki et al. (2016) via microlens.

Table 3. Best fit parameters of the mass function for the planetary mass population.

	CR1	CR2		Gould+22
$(M_{\rm norm})$	$(8\ M_\oplus)$	$(8\ M_\oplus)$	$(38\ M_\oplus)$	$(38\ M_\oplus)$
M_1	(0.86)	(0.86)		
α_1	(1.32)	(1.32)		
α_2	(0.13)	(0.13)		
α_3	$-0.55^{+0.13}_{-0.17}$	$-0.58^{+0.12}_{-0.16}$		
α_4	$0.90^{+0.48}_{-0.27}$	$0.96^{+0.47}_{-0.27}$		fixed at 0.9 or 1.2
Z	$2.08^{+0.54}_{-1.33}$	$2.18^{+0.52}_{-1.40}$	$0.49^{+0.17}_{-0.37}$	
$Z_{\rm MS+BD}$	$2.27^{+0.60}_{-1.46}$	$2.38^{+0.58}_{-1.53}$	$0.53^{+0.19}_{-0.40}$	$0.39\pm0.20\pm?$
$Z^{M_\odot}$	$5.33^{+1.26}_{-3.40}$	$5.48^{+1.18}_{-3.50}$	$1.22^{+0.35}_{-0.91}$	
$Z^{M_\odot}_{\rm MS+BD}$	$10.63^{+2.52}_{-6.78}$	$10.95^{+2.36}_{-6.97}$	$2.44^{+0.71}_{-1.82}$	$1.96\pm0.98\pm?$
f [a]	17^{+20}_{-11}	21^{+23}_{-13}		
$f_{\rm MS+BD}$ [a]	19^{+22}_{-12}	23^{+25}_{-15}		
$f^{M_\odot}$ [a]	45^{+54}_{-30}	53^{+59}_{-34}		
$f^{M_\odot}_{\rm MS+BD}$ [a]	89^{+107}_{-59}	106^{+117}_{-68}		
m [b]	$89^{+96}_{-56}M_\oplus$	$80^{+73}_{-47}M_\oplus$		
$m_{\rm MS+BD}$ [b]	$98^{+107}_{-61}M_\oplus$	$88^{+81}_{-51}M_\oplus$		
$m^{M_\odot}$ [b]	$229^{+219}_{-140}M_\oplus$	$202^{+166}_{-114}M_\oplus$		
$m^{M_\odot}_{\rm MS+BD}$ [b]	$457^{+439}_{-279}M_\oplus$	$404^{+333}_{-228}M_\oplus$		
χ^2	36273.0	36024.1		

[a] Number of planetary mass objects per BD+MS+WD (f), per MS+BD ($f_{\rm MS+BD}$), per solar mass of BD+MS+WD ($f^{M_\odot}$) or per solar mass of MS+BD ($f^{M_\odot}_{\rm MS+BD}$) when MF down to $10^{-6}M_\odot$ are integrated. These are vary depending on the minimum mass.

[b] Total mass of planetary mass objects per BD+MS+WD (m), per MS+BD ($m_{\rm MS+BD}$), per solar mass of BD+MS+WD ($m^{M_\odot}$) or per solar mass of MS+BD ($m^{M_\odot}_{\rm MS+BD}$) when MF down to $10^{-6}M_\odot$ are integrated.

NOTE—We adopt the model for CR2 as the final result.

13 events with strong finite source effects that allow the determination of the angular Einstein radius, $\theta_{\rm E}$.

The cumulative $\theta_{\rm E}$ histogram for these 13 events reveals an "Einstein gap" at $5<\theta_{\rm E}/\mu{\rm as}<70$ which is roughly consistent with the gap at $10<\theta_{\rm E}/\mu{\rm as}<30$ found by the KMTNet group (Ryu et al. 2021; Gould et al. 2022). This gap indicates that there is a distinct planetary mass population separated from the known populations of brown dwarfs, stars and stellar remnants.

We constructed the $t_{\rm E}$ distribution of all selected samples including both PSPL and FSPL. We calculated the integrated detection efficiency $\tilde{\epsilon}(t_{\rm E};\Gamma)$ of the survey by integrating the two dimensional detection efficiency, $\epsilon(t_{\rm E},\theta_{\rm E})$, measured from image level simulations that included the FS effect, and convolving this with the event rate $\Gamma(t_{\rm E},\theta_{\rm E})$ given by a Galactic model and MF. We found that the $t_{\rm E}$ distribution has an excess at short

$t_{\rm E}$ values which can not be explained by known populations.

We then adopted the power law MF for the planetary mass population. We found that these short events can be well modeled by $dN_4/d\log M = (2.18^{+0.52}_{-1.40}) \times (M/8\,M_\oplus)^{-\alpha_4}$ dex^{-1}star^{-1} with $\alpha_4 = 0.96^{+0.47}_{-0.27}$ at $10^{-7} < M/M_\odot < 0.02$ (or $0.033 < M/M_\oplus < 6660$).

This can also be expressed by the MF per stellar mass as, $dN_4/d\log M = 5.48^{+1.18}_{-3.50} \times (M/8\,M_\oplus)^{-\alpha_4}$ dex$^{-1}M_\odot^{-1}$. We showed the number of FFP or distant planets is $f = 21^{+23}_{-13}$ per stars.

It is well known that planet-planet scattering during the planet formation process is likely to produce a population of unbound or wide orbit planetary mass objects (Rasio & Ford 1996; Weidenschilling & Marzari 1996; Lin & Ida 1997) The probability of planet scattering likely increases with declining mass because planets usually require more massive planets to scatter. So, we expect the power law index of MF of bound planets $\alpha_{\rm b}$ is smaller than that of α_4 for unbound or large orbit planets, i.e., $\alpha_4 > \alpha_{\rm b}$.

One can compare our FFP result to the MF of known bound planets. At present, microlensing surveys have only measured the mass ratio function, rather than the mass function, of the bound planets. Currently, the most sensitive study of the bound planet mass ratio function Suzuki et al. (2016) found that the mass ratio function can be well explained by the broken power law with $\alpha_{\rm b} = 0.93 \pm 0.13$ for $q > q_{\rm br} = 1.7 \times 10^{-4}$, $\alpha_{\rm b} = -0.6^{+0.4}_{-0.5}$ for $q < q_{\rm br} = 1.7 \times 10^{-4}$. While the Suzuki et al. (2016) data could establish the existence of the power-law break with reasonably high confidence (a Bayes factor of 21), there was a large, correlated uncertainty in the mass ratio of the break and slope of the mass ratio function below the break. So, we chose to fix the mass ratio of break at $q_{\rm br} = 1.7 \times 10^{-4}$ in order to estimate the power law below the break.

More recently, several papers have attempted to improve upon this estimate by including a heterogeneous set of lower mass ratio planets found by a number of groups without a calculation of the detection efficiency. These efforts included attempts to estimate the effect of a "publication bias" that might cause planets deemed to be of greater interest to be published much more quickly, leading to biased, inhomogeneous sample of planets. This "publication bias" is caused by the decision to publish some planet discoveries at a higher priority than others. With such an analysis Udalski et al. (2018) reported $\alpha_{\rm b} = -1.05^{+0.68}_{-0.78}$ with their sample and $\alpha_{\rm b} = -0.73^{+0.42}_{-0.34}$ when combined with the Suzuki et al. (2016) result for $q < 1 \times 10^{-4} < q_{\rm br}$. A similar analysis by Jung et al. (2019), attempted a new measurement of the location of the break and found $\alpha_{\rm b} = -4.5$ for $q < q_{\rm br} = 0.55 \times 10^{-4}$ which is consistent with the Suzuki et al. (2016) result when $q_{\rm br}$ is not fixed. However, a more recent paper (Zang et al. 2022) by many of the same authors, reported a number of planetary microlensing events that were missed by the analyses described in Udalski et al. (2018) and Jung et al. (2019). This casts some doubt on the validity of some of the assumptions in these papers. This later paper also suggests that planets with mass ratios of $q < q_{\rm br} = 1.7 \times 10^{-4}$ may be more common than previously thought, although a more definitive claim awaits a detection efficiency calculation. Also, the Suzuki et al. (2016) analysis does not imply that there is a peak in the mass ratio. Instead it concludes that the slope does not rise as steeply toward low mass ratios as is does for $q > 1.7 \times 10^{-4}$.

The broken power-law model of Suzuki et al. (2016) is consistent with the hypothesis that these unbound or wide orbit planetary mass objects are the result of scattering from bound planetary systems. It is the lower mass planets that are preferentially removed by planet-planet scattering interactions, so the initial planetary mass function may have been closer to a single power-law with $\alpha_{\rm b} \sim 0.9$, but planet-planet scattering has likely depleted the numbers of low-mass planets at separations beyond the snow line where microlensing is most sensitive. Thus, planet-planet scattering may be responsible for the mass ratio function "break" observed in the Suzuki et al. (2016) sample

This idea that planet-planet scattering is responsible for a FFP mass function slope that is steeper than the slope of the mass ratio function for low-mass bound planets is also consistent with the single power-law models that were found in smaller data sets (Sumi et al. 2010). The best fit single power-law model for the Suzuki et al. (2016) sample gives $dN_{\rm bound}/d\log q = 0.068^{+0.016}_{-0.014}$dex^{-2}star$^{-1} \times (q/0.001)^{-\alpha_{\rm b}}$ with $\alpha_{\rm b} = 0.58 \pm 0.08$ for $3 \times 10^{-6} < q < 3 \times 10^{-2}$, but the broken power-law is a significantly better fit to the Suzuki et al. (2016) data. Note, this single power law model with $\alpha_{\rm b} = 0.58$ satisfies $\alpha_4 > \alpha_{\rm b}$, for our value of $\alpha_4 = 0.96^{+0.47}_{-0.27}$, implying that unbound (or very wide orbit) planets increase more rapidly than bound planets at low masses. Thus our main conclusion discussed bellow with the broken power law model, which the lower mass planets are increasingly scattered, is not specific to the Suzuki et al. (2016) broken power-law model.

As a comparison, we transformed the bound planet's mass "ratio" function of Suzuki et al. (2016) to a mass function by using the estimated average mass of their

hosts of $\sim 0.56 M_\odot$ as shown[2] in Figure 6. We estimate the abundance of the wide-orbit bound planets to be $f_{\rm wide} = 1.1^{+0.6}_{-0.3}$ planets star^{-1} in the mass range $10^{-6} < M/M_\odot < 0.02$ ($0.33 < M/M_\oplus < 6660$) and separation range $0.3 < s < 5$, which corresponds to a semi-major axis of roughly $0.7 < a/{\rm au} < 12$. This indicates that the abundance of FFP, $f = 21^{+23}_{-13}$ planets star^{-1}, is 19^{+23}_{-13} times more than wide-orbit bound planets in this mass range.

This is because the number of wide-orbit bound planets decreases at lower masses than the break at $M_{\rm break} \approx 1.0 \times 10^{-4} M_\odot$, while the number of high-mass bound planets is larger than that for FFP. Again, this is consistent with the hypothesis that the low-mass planets are more likely to be scattered. Note that there is still large uncertainty in the MF at low masses for both bound and unbound planets. It is very important to constrain the these MFs at low masses.

We can also compare our number for the FFP abundance with the abundance of the bound planets with short period orbits of $P = 0.5 - 256$ days and planetary radii of $R_{\rm p} = 0.5 - 4R_\oplus$ found by Kepler. Hsu, Ford, Ragozzine & Ashby (2019) find $f_{\rm FGK} = 3.5^{+0.7}_{-0.6}$ for FGK dwarfs and Hsu, Ford & Terrien (2020) find $f_{\rm M} = 4.2^{+0.6}_{-0.6}$ for M dwarfs. Because the typical spectral types of their samples are G2 ($M = 1M_\odot$) and M2.5 ($M = 0.4M_\odot$), their typical semi-major axis are $0.012 \lesssim a/{\rm au} \lesssim 0.79$ and $0.009 \lesssim a/{\rm au} \lesssim 0.58$, respectively. The fraction of FGK and M dwarfs relative to all population except BH and NS are 0.157 : 0.465 in our best fit MF. By weighting with these stellar type fractions, the abundance of the known close-orbit bound planets is about $f_{\rm close} = 2.5^{+0.3}_{-0.3}$ per star. (This ignores the relatively small number of gas giant planets in short period orbits (Bryant et al. 2023)).

The total abundance of the wide-orbit and known close-orbit bound planets is about $f_{\rm bound} = 3.6^{+0.7}_{-0.4}$ per star. This indicates that the abundance of FFP, $f = 21^{+23}_{-13}$ planets star^{-1}, is $5.8^{+6.4}_{-3.8}$ times more than known bound planets in this mass range.

We found the total mass of FFPs or distant planets per star is $m = 80^{+73}_{-47} M_\oplus (0.25^{+0.23}_{-0.15} M_{\rm J})$ star^{-1} in this $10^{-6} < M/M_\odot < 0.02$ ($0.33 < M/M_\oplus < 6660$) mass range. This is comparable to the value of $91^{+33}_{-22}\ M_\oplus$ star^{-1} for wide-orbit bound planets with separations of $0.3 < s < 5$ in the same mass range. It is not straight forward to estimate the total mass of inner planet found by Kepler because only a small, and somewhat biased, sample of Kepler planets have mass measurements. The total masses of FFP and bound planets are less dependent on the uncertainty of the number of low mass planets than the total numbers of FFP and bound planets are.

These comparisons indicate that 19^{+23}_{-13} times more planets than the ones currently in wide orbits have been ejected to unbound or very wide orbits. These comparisons also suggest that the total mass of scattered planets is of the same order as those remaining bound in wide orbits (beyond the snow line) in their planetary systems. The low mass bound planets in wide orbits are much less abundant than those orbiting closer to their host stars. This may be explained by that planets in wide orbits are more easily ejected than those in close orbit.

The power-law index of the IMF of planets formed in wide orbits in protoplanetary disks is likely to be $\alpha_4 \sim 0.9$ with an abundance of 22^{+23}_{-13} planets star^{-1} or $171^{+80}_{-52} M_\oplus (0.54^{+0.25}_{-0.16} M_{\rm J})$ star^{-1}.

Another, rather speculative, possibility is that most of the low-mass objects found by microlensing are primordial black holes (PBH). Hashino et al. (2022) predicted PBH generated at a first order electroweak phase transition have masses of about $10^{-5} M_\odot$. They found that depending on parameters of the phase transition a sufficient number of PBH can be produced to be observed by current and future microlensing surveys. The mass of such PBH is a function of the time of their generation, i.e., the electroweak phase transition, and is expected to be a delta-function distribution. To differentiate PBH from FFP, we need to measure the shape of the MF accurately. This can be done by the current (MOA, OGLE, KMTNet) surveys, the near future (PRIME) ground telescope and the Roman Space telescope.

For the first time, we have determined the detection efficiency as a function of both the Einstein radius crossing time and the angular Einstein radius, because finite source effects have a large influence on the detectability of microlensing events due to low-mass planets. This method is necessary for reliable results for low-mass FFPs, and it should be very useful for the analysis of these future surveys which will detect many short events.

A precise measurement of the free floating planet mass function will require a microlensing survey that can obtain precise photometry of main sequence stars with relatively low magnification, because the small angular Einstein radii, $\theta_{\rm E}$, of low-mass planetary lenses prevent high magnification. The exoplanet microlensing survey of the Roman Space Telescope is such a survey, and it

[2] The 1σ range indicated by the gray shaded area in Figure 6 does not match the one provided in Suzuki et al. (2016). This was due to an error in the Suzuki et al. (2016) figure, but there is no error in the other results in that paper.

should provide the definitive measurement of the free floating planet mass function.

We are grateful to ** for helpful comments. The MOA project is supported by JSPS KAKENHI Grant Number JSPS24253004, JSPS26247023, JSPS23340064, JSPS15H00781, JP16H06287, JP17H02871 and JP22H00153. NK was supported by the JSPS overseas research fellowship. DPB acknowledges support from NASA grants 80NSSC20K0886 and 80NSSC18K0793.

REFERENCES

Agol, E. 2003, ApJ, 594, 449

Bennett, D. P., Rhie, S. H., Nikolaev, S., et al. 2010, ApJ, 713, 837

Bennett, D. P., Sumi, T., Bond, I. A., et al. 2012, ApJ, 757, 119

Boss, A. P., Basri, G., Kumar, S. S., et al. 2003, Brown Dwarfs, 211, 529

Bozza V., Bachelet, E., & Bartolić, F., et al., 2018, MNRAS, 479, 5157

Bryant, E. M., Bayliss, D., & Van Eylen, V. 2023, arXiv:2303.00659. doi:10.48550/arXiv.2303.00659

Gaudi, B. S., Bennett, D. P., Udalski, A., et al. 2008, Science, 319, 927

Gould, A. et al. 2022, Journal of the Korean Astronomical Society, 55, 173

Han, C. & Gould, A. 1996, ApJ, 467, 540. doi:10.1086/177631

Hashino, K., Kanemura, S., & Takahashi, T. 2022, Physics Letters B, 833, 137261. doi:10.1016/j.physletb.2022.137261

Hogg, D. W., Myers, A. D., & Bovy, J. 2010, ApJ, 725, 2166. doi:10.1088/0004-637X/725/2/2166

Holtzman, J. A., Watson, A. M., Baum, W. A., et al. 1998, AJ, 115, 1946

Hsu, D. C., Ford, E. B., Ragozzine, D.& Ashby, K. 2019, AJ, 158, 109

Hsu, D. C., Ford, E. B., Terrien, R. 2020, MNRAS, 498, 2249

Jung, Y. K., Gould, A., & Zang, W., et al. 2019, AJ, 157, 72

Kim, H.-W., Hwang, K.-H., Gould, A., et al. 2021, AJ, 162, 15

Koshimoto, N., Baba, J., & Bennett, D. P. 2021a, ApJ, 917, 78. doi:10.3847/1538-4357/ac07a8

Koshimoto, N., Bennett, D. P., Suzuki, D., et al. 2021b, ApJL, 918, L8. doi:10.3847/2041-8213/ac17ec

Koshimoto, N., Sumi, T. and Bennett, D. P., et al. 2023, ApJ, submitted (K23)

Lam, C. Y., Lu, J. R., Hosek, M. W., et al. 2020, ApJ, 889, 31. doi:10.3847/1538-4357/ab5fd3

Lin, D. N. C. & Ida, S. 1997, ApJ, 477, 781. doi:10.1086/303738

Maeder, A. 1973, A&A, 26, 215

Mao, S., & Paczyński, B. 1991, ApJ, 374, L37

Metropolis, N., Rosenbluth, A. W., Rosenbluth, M. N., Teller, A. H., & Teller, E. 1953, JChPh, 21, 1087

Mróz, P. Udalski A., Skowron, J., et al. 2017, Nature, 548, 183

Mróz, P. Y.-H.Ryu, Skowron, J., et al. 2018, ApJ, 155, 121

Mróz, P. Udalski A., Skowron, J., et al. 2019, ApJS, 244, 29

Mróz, P. Udalski A., Bennett, D. P. et al. 2019, å, 622, A201

Mróz, P. Udalski A., Szymański, M., et al. 2020, ApJS, 249, 16

Mróz, P., Poleski, R. & Gould, A. 2020, ApJ, 903, 11

Mróz, P., Poleski, R., Han, C. 2020, AJ, 159, 262

Paczyński, B. 1986, ApJ, 304, 1

Paczyński, B. 1991, ApJ, 371, L63

Rasio, F. A. & Ford, E. B. 1996, Science, 274, 954. doi:10.1126/science.274.5289.954

Riffeser, A., Fliri, J., Seitz, S., & Bender, R. 2006, ApJS, 163, 225

Ryu, Y-H, Mróz, P., Gould, A. 2021, AJ, 161, 126

Sumi, T. et al., 2003, ApJ, 591, 204

Sumi, T. et al., 2010, ApJ, 710, 1641

Sumi, T. et al., 2011, Nature, 473, 349

Sumi, T. Bennett, D. P. & Bond I. A. et al., 2013, ApJ, 778, 150

Sumi, T., Udalski, A., & Bennett, D. P. et al., 2016, ApJ, 825, 112

Suzuki, D. Bennett, D. P. & Sumi T. et al., 2016, ApJ, 833, 145

Udalski, A. et al. 1994, Acta Astronomica, 44, 165

Szymański, M., Udalski, A. & Soszyński I. et al. 2011, Acta Astronomica, 61, 83

Udalski,A., Ryu, Y.-H., Sajadian, S., et al. 2018, AcA, 68, 1

Weidenschilling, S. J. & Marzari, F. 1996, Nature, 384, 619. doi:10.1038/384619a0

Zang, W., Yang, H., Han, C., et al. 2022, MNRAS, 515, 928. doi:10.1093/mnras/stac1883